# 2 Phase Control of Molecular System Project

## – Structural investigations of molecular systems under external conditions –

*Project Leader: Reiji Kumai*

In this project, electronic correlation in molecular crystal systems is being investigated to elucidate novel phenomena such as superconductivity, ferroelectricity and charge ordering. One of our goals is to elucidate the origins of physical properties from crystal structural information. For this purpose, we performed crystal structure analysis of various molecular systems including organic thin films under external conditions.

In the first period of the CMRC, we conducted many structural studies on organic ferroelectrics. Recently we succeeded in making a high-quality thin film of organic ferroelectric and evaluated it by using the diffraction of synchrotron radiation as follows.

In addition, we started the commissioning of the thin film diffractometer installed in BL-7C, Photon Factory, KEK. This will accelerate the structural investigation of thin films.

### 2-1 Proton Tautomerism for Strong Polarization Switching [1]

Ferroelectrics are electrically polar substances in which the direction of spontaneous polarization is reversibly switchable under the influence of an external electric field. Organic systems are free of both toxic and rare elements, well suited to highly productive printing into sheet devices, and are expected to be advantageous for emerging applications with cheap, disposal, flexible, wearable, and/or implantable characteristics. Recently, some small organic molecules have appeared as future potential alternatives: molecules in which proton transfer within the hydrogen bonds can invert the crystal polarity under much lower switching fields typically ranging from one to several tens of kilovolts per centimeter. Therefore, few-volt switching has been achieved even on printed micrometer-thick single-crystal films of 2-methylbenzimidazole (MBI) [2].

Among ferroelectric small molecules, croconic acid (CRCA) [3] has generated the strongest polarization through a cooperative proton tautomerism mechanism (called prototropy, abbreviated herein as PTM), which relocates a proton through the hydrogen bond and simultaneously interchanges the locations of a single bond and adjacent double bond (Fig. 1). This discovery was followed by the development of PTM ferroelectrics using the β-diketone enol O=C–C=C–OH moieties, carboxylic acid O=C–OH moiety, and heterocyclic –N=C–NH– moieties. All these PTM ferroelectric crystals construct extended chains of intermolecular resonance-assisted hydrogen bonds (RHAB), which are strengthened by the interplay with the conjugated π-bond system.

Despite having excellent prospects, many organic ferroelectric crystals including those based

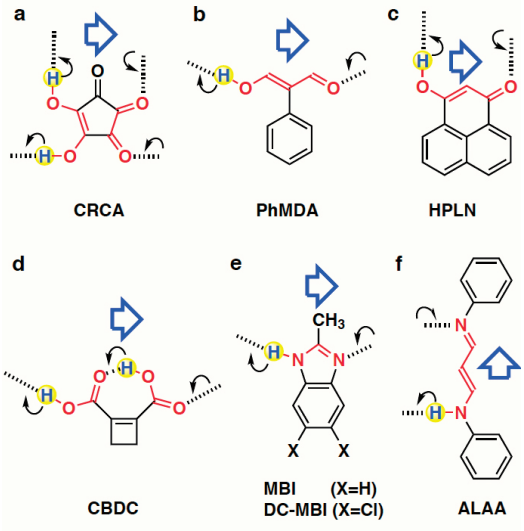


**Fig. 1:** Chemical structural mechanisms of ferroelectric proton tautomerism (PTM).

on PTM have often exhibited some ambiguity in actual performance; polarization–electric field (*P*–*E*) hysteresis loops are often ill-shapen, and the much-lower-than-expected remanent polarization values depend strongly on pristine crystals. In general, ferroelectric crystals adopt a multidomain structure in which ferroelectric domain walls (DWs) separate differently polarized sections (domains) and their sweeping motion changes the bulk polarization. DW pinning is expected for solution-grown PTM ferroelectric crystals, because their Curie point is above room temperature or even beyond the thermal stability limit of the solid state. Previous *P*–*E* hysteresis measurements of CRCA exploited both thermal annealing and repetitive switching for depinning DWs, although poor reproducibility of the best polarization (21 μC cm$^{-2}$) suggested that these procedures are still insufficiently optimized.

Here, we revise the *P*–*E* hysteresis properties of solution-grown PTM ferroelectric crystals by finding effective optimization procedures. The optimized remanent polarizations ($P_r$) were evaluated in comparison with the results of first-principles calculations. We considered the cooperative roles of proton transfer and π-bond switching using the ion-displacive (point-charge) picture and hydrogen-bond geometry. Seven PTM ferroelectric compounds including a new compound allow for a systematic understanding of polarization in search of design principles for high-performance switching.

Our previous studies have discovered six PTM ferroelectrics: CRCA, PhMDA, HPLN, CBDC, MBI, and DC-MBI. All these crystal structures comprise extended one- or two-dimensional networks through intermolecular hydrogen bonds; O–H---O bonds for the former four compounds and N–H---N bonds for the latter two. As shown schematically in Fig. 1, the polarity of the hydrogen-bonded networks is switchable through cooperative proton transfer and concomitant interchange of the double- and single-bond locations. In addition, the crystallographic requirement for ferroelectricity is a hidden pseudo-symmetry, which would survive as a paraelectric configuration.

Here, we also report a new N–H---N bonded compound as the seventh PTM ferroelectric: 3-anilinoacrolein anil (ALAA), which was encountered in the Cambridge Structural Database (CSD) (Refcode: ANPHPR). Because this entry does not include the atomic coordinates for the hydrogen atom, we have re-examined the crystal structure at room temperature ($T$ = 295 K). The crystal structure belongs to the orthorhombic system with the polar space group *Iba*2 (#45) in agreement with the report. The crystal polarity is parallel to the crystal *c*-axis, which is along the direction in which the hydrogen bonds construct an infinite chain of twists and turns. Without the N–H proton and π-bond alternation, the molecule can restore the pseudo-twofold rotation symmetry and occupy the $C_2$-site so as to constitute the centric (hypothetical) paraelectric structure: the space group *Ibca* (#73). Although the hydrogen-bonded chain

**Table 1:** Experimental and calculated polarization of PTM ferroelectric crystals.

| Compound | Polarization (μC cm$^{-2}$) | | | | | | Direction | Local dipole moment |
|---|---|---|---|---|---|---|---|---|
| | Experimental | | Theoretical (Berry) | | Point charge model | | component | of proton transfer |
| | $\lvert\mathbf{P}^{exp}\rvert$ | $(P_x, P_y, P_z)^{exp}$ | $\lvert\mathbf{P}^{cal}\rvert$ | $(P_x, P_y, P_z)^{cal}$ | $\lvert\mathbf{P}^{ion}\rvert$ | $(P_x, P_y, P_z)^{ion}$ | $(x, y, z)$ | $\lvert\boldsymbol{\mu}\rvert$ (10$^{-30}$ C m) |
| **1**. CRCA | 30 | (0, 0, 30) | 29.4 | (0, 0, 29.4) | 5.5 | (0, 0, 5.5) | $(a, b, c)$ | 4.4, 5.0 |
| **2**. PhMDA | 9 | (0, 0, 9) | 9.0 | (0, 0, 9.0) | 1.8 | (0, 0, 1.8) | $(a, b, c)$ | 5.3 |
| **3**. HPLN | 5.6 [b] | – | 5.2 | (−5.2, 0, −0.1) | 2.5 | (0, 0, 0) | $(a, b, c^*)$ | 5.9, 6.0 |
| | | 4.5 | | 4.2 | | | $\perp(10\bar{1})$ | |
| **4**. CBDC | 13.2 | (8.6, 0, −10.0)[a] | 15.1 | (11.7, 0, −9.6) | 6.7 | (6.3, 0, −2.2) | $(a, b, c^*)$ | 5.5 |
| **5**. MBI | 7.4 [b] | – | 7.1 | (−0.2, 0, −7.1) | 2.5 | (−0.2, 0 −2.5) | $(a, b, c^*)$ | 6.7, 5.7, 6.7, 6.1 |
| | | 5.2 | | 5.0 | | | ∥[101] | |
| **6**. DC-MBI | 10 | (0, 0, −10) | 10.0 | (0, 0, −10.0) | 3.8 | (0, 0, 3.8) | $(a, b, c)$ | 8.3 |
| **7**. ALAA | 3.6 | (0, 0, 3.6) | 4.2 | (0, 0, 4.2) | 0.6 | (0, 0, 0.6) | $(a, b, c)$ | 7.5 |

[a] Because the sign of each direction component of $\mathbf{P}^{exp}$ could not be identified by the *P*–*E* hysteresis experiments alone, it is assumed to be the same as that of $\mathbf{P}^{cal}$.

[b] The direction of the applied field exhibits a certain inclination angle from the polarization vector. The total amplitude of experimental polarization $\lvert\mathbf{P}^{exp}\rvert$ was derived in consideration of this (theoretical) angle

acquires a dipole switchable with the proton location, its polarization should mostly arise from the switchable $\pi$-bond dipole because all the protons travel in a direction normal to the polar axis. The orthogonality of the chain dipole and the proton's path is similar to the case of the HPLN crystal (see Fig. 1).

According to the current dielectrics theory of solids, the evaluation of macroscopic polarization through the Berry phase formalism demands precise knowledge of the electronic structures in the crystal form. Therefore, for all seven ferroelectrics, first-principles electronic structure calculations were performed to evaluate the spontaneous polarization $\mathbf{P}^{cal}$. The $\mathbf{P}^{cal}$ values of the CRCA and CBDC crystals are close to the corresponding theoretical predictions: ($P_a$, $P_b$, $P_c$) = (0, 0, 26.0) μC cm$^{-2}$ for CRCA and ($P_a$, $P_b$, $P_c$*) = (12.7, 0, −6.6) μC cm$^{-2}$ for CBDC. These values change slightly depending on the details of the computational conditions such as the structural parameters and the exchange-correlation functional. In Table 1, we compare the theoretical polarizations $\mathbf{P}^{cal}$ with the *P*–*E* hysteresis data $\mathbf{P}^{exp}$. For the PhMDA, MBI, and DC-MBI crystals, the remanent polarizations listed are those of the previous report and agree well with the corresponding theoretical polarizations. Since all these crystals were commonly grown from a high-temperature vapor phase, the thermal annealing effect is likely to have maximized the performance by eliminating pinned DWs. In fact, PFM images of MBI crystals revealed only neutral 180° and 90° DWs rather than charged DWs.

However, for all the solution-processed as-grown single crystals, the $\mathbf{P}^{cal}$ values (see Table 1) are much larger than previously reported values. The present re-examinations have reinforced the maximum amplitude ($E_{max}$) of the bipolar electric field, which was hitherto set to less than 33 kV cm$^{-1}$ for a triangular waveform so as to avoid an electric discharge between electrodes on the crystal surface. Satisfactory optimization has been accomplished for crystals immersed in silicone oil with field amplitudes increased up to 33–100 kV cm$^{-1}$ using rectangular-pulse voltages. Earlier work on a CRCA crystal increased $P_r$ up to 21 μC cm$^{-2}$ by applying 600 cycles of a 1 Hz triangular-wave voltage of $E^{max}$ = 33 kV cm$^{-1}$ followed by thermal annealing at 400 K. Here, we applied bipolar rectangular-pulse voltages of a stronger field amplitude (pulse field amplitude $E^{puls}$ = 33–55 kV cm$^{-1}$) to four specimens of different initial $P_r$ ranging from 2 to 13 μC cm$^{-2}$. Gradual expansion of the hysteresis loops with an increasing number of pulses corresponds to the so-called wake-up process. After a few ten thousand pulses, the $P_r$ reproducibly reached a maximum as high as 28–32 μC cm$^{-2}$. This optimum $P_r$ is in excellent agreement with our theoretical evaluation (29.4 μC cm$^{-2}$). Moreover, the switchable polarization breaks its own record for organic ferroelectrics by increasing from 21 to about 30 μC cm$^{-2}$ and has just exceeded the performance of some commercial ferroelectric materials such as $BaTiO_3$ and $SrBi_2Ta_2O_9$ (20–26 μC cm$^{-2}$). Polarizations of the $\alpha$-form HPLN crystal and CBDC crystal were improved with both thermal heating and repetitive switching. The ALAA crystal, which was newly grown from ethanol solution, also exhibited ferroelectricity in the *P*–*E* hysteresis experiments with an **E**||*c* configuration, in agreement with the structural assessment above. The remanent polarization was similarly optimized to a modest value (3.6 μC cm$^{-2}$) after applying 3 × 10$^4$ cycles of triangular-waveform voltages ($E^{max}$ = 60 kV cm$^{-1}$). The ferroelectric state is stable at least up to the melting point at 388 K, below which the signature of the phase transition was absent until room temperature according to a thermal analysis using a high sensitivity differential scanning calorimeter.

For the solution-processed as-grown PTM ferroelectric crystals, the switchable polarization has been "woken up" by repetitive switching with an increased amplitude of the bipolar field rather than by improving the crystal quality. Hence, most of the pinning sites are not permanently clamping impurities or defects. Rather, they are charged DWs with compensating charges trapped nearby and can be gradually moved away under the influence of a strong electric field. All the solution-processed as-grown PTM ferroelectric crystals herein have been finally optimized with significant improvement of their spontaneous polarization. In comparison with the corresponding earlier data, the improved performance is also evident by the optimized *P*–*E* curvatures themselves. Good rectangularity of the loop and frequency independence of $P_r$ suggested the almost complete removal of charged DWs and successfully revealed the materials' actual properties.

Figure 2a plots the best experimental performance |$\mathbf{P}^{exp}$| of the seven PTM compounds as a

function of the theoretical polarization amplitude $|\mathbf{P}^{cal}|$. Because the applied field **E** is inclined with respect to the predicted $\mathbf{P}^{cal}$ for the HPLN and MBI crystals, each measured $\mathbf{P}^{exp}$ was corrected to the total amplitude $|\mathbf{P}^{exp}|$ considering this inclination angle. Note that the polarizations vary widely from 3.6 to 30 μC cm$^{-2}$. After the optimization and correction, all the experimental data fall near the linear line $|\mathbf{P}^{exp}| = |\mathbf{P}^{cal}|$, and the largest discrepancy, found for the ALAA and CBDC crystals, is only 14–15%.

During the switching with PTM, the protons travel ~0.6–1.0 Å within the hydrogen bond. This classical picture suggests significant ionic polarization. The line graph in Fig. 2b actually reveals a trend that shows the total polarization $|\mathbf{P}^{cal}|$ (solid diamonds) increasing with proton density (solid squares). We first estimate this electrostatic contribution from protons displacing among molecular (anionic) cores. In the point-charge model, the ionic polarization $\mathbf{P}^{ion}$ is expressed as

$$\mathbf{P}^{ion} = \Sigma_{(cell)}\, Z_i\, |e|\, \mathbf{u}_i/\Omega$$

where $e$ is the electron charge, $\mathbf{u}_i$ is the relative displacement of the static charges $Z_i\,|e|$, $\Omega$ is the unit cell volume, and $Z_i$ is taken as +1 for protons and –1 or –2 for molecular cores.

In the histogram in Fig. 2b, each total polarization $\mathbf{P}^{cal}$ was divided into $\mathbf{P}^{ion}$ (red bar) and a remainder contribution (blue bar). Each molecule of CRCA or CBDC accommodates two protons in the compact molecular size, and the resulting large proton density amplifies $\mathbf{P}^{ion}$. However, $\mathbf{P}^{ion}$ is still less than half of $\mathbf{P}^{cal}$ in amplitude, indicating the addition of some larger contributions.

Our success in efficiently optimizing ferroelectric switching has reduced the discrepancy of the polarization with the results of the first-principles calculations to less than 15%. Thus, one of the important outcomes of this work is evidence of the practicality of the calculations, which will be useful for predicting the experimentally unknown performance of similar organic systems for which the precise crystal structure is known. It should be noted that evaluation of the ferroelectricity as well as the theoretical polarizations require careful diffraction studies.

The PTM ferroelectrics studied herein exhibited a stable ferroelectric state up to temperatures well above room temperature even until the stability limit of the crystals themselves, such as the melting, decomposition, or sublimation temperatures. Two issues are relevant to this thermal stability. The first is the necessity of the depinning process for the solution-processed as-grown crystals. This is because the solution process, at far below the Curie point, spontaneously grows polarized crystals of a multidomain structure (i.e. twinning) and embeds charged DWs frozen therein. The second is the excellent consistency between the experimental and simulated polarizations. One of the reasons for this is the deep potential minima in the fully polarized state, which minimized the ambiguity in the proton locations once accurate positions of the non-hydrogen atoms were experimentally determined.

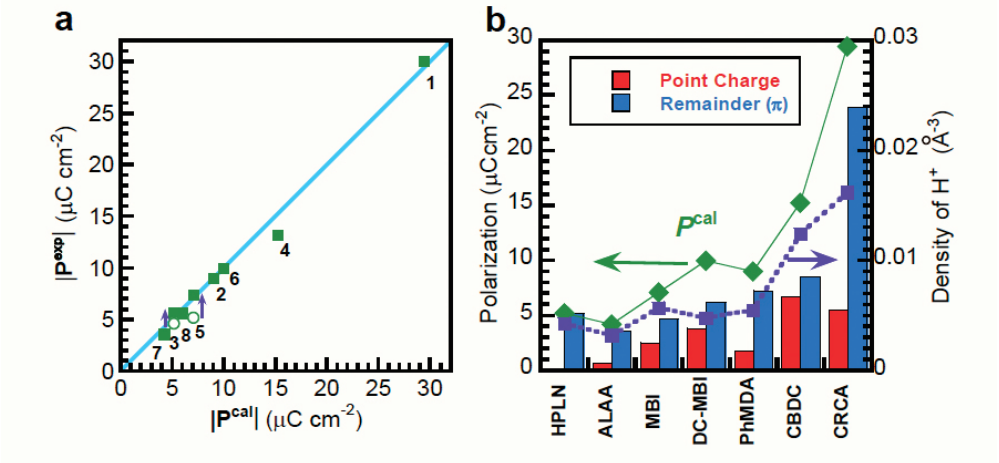


**Fig. 2:** Comparison of spontaneous polarizations of PTM ferroelectrics. (a) The experimentally optimized performance $|\mathbf{P}^{exp}|$ versus calculated total polarization $|\mathbf{P}^{cal}|$ of the CRCA (1), PhMDA (2), HPLN (3), CBDC (4), MBI (5), DC-MBI (6), and ALAA (7) crystals along with anthranilic acid I (8). (b) Calculated total polarizations $|\mathbf{P}^{cal}|$ (green diamonds) divided into ionic polarizations $|\mathbf{P}^{ion}|$ of displacing protons estimated under the point-charge approximation (red histogram) and the remainder contribution (blue histogram). Purple squares denote the volume density of protons in the crystal. Dotted and solid lines are guides for the eye.

The structure–property relationship together with the point-charge-model analysis yielded some molecular and crystal design strategies for higher-performance PTM ferroelectrics. The first issue concerns the direction of each contributing dipole moment. The total polarization $\mathbf{P}^{cal}$ was described by the accumulation of the ionic contribution $\mathbf{P}^{ion}$ from the proton displacement and the larger remaining contributions mainly from switchable $\pi$-bond dipoles. These cumulative contributions to the polarization are the converse of the subtractive nature in intramolecular hydrogen-bonded PTM such as 9-hydroxyphenalenone: the $\pi$-bond dipole changes in the opposite direction to that of the relocating protons, and some cancellation yields tiny switchable molecular dipoles (0.4 D ~ $1.3 \times 10^{-30}$ C m) compared with the local dipole moment around the hydrogen atom. In contrast, the extended chains of intermolecular hydrogen bonds are ideal for enlarging the polarization, especially when both the local proton motion and the change in the $\pi$-bond dipoles are nearly aligned parallel to the polar crystal axis. This requirement is well satisfied in CRCA, CBDC, and DC-MBI crystals.

The second issue is the density of dipoles. As noted above, the total polarization actually increases with increasing proton density. Similarly, one can easily envisage that the corresponding strategy for switchable $\pi$-bond dipoles is to increase the volume fraction of PTM fragments, which are shown in red in Fig. 1. As a typical case, the dibasic acids CRCA and CBDC are similar in terms of the ionic contribution $\mathbf{P}^{ion}$ and the proton density, but the remainder contribution in CRCA is huge and about three times as large as that of CBDC. The reason for this can be understood qualitatively in that the only fragment irrelevant to PTM is one C=O unit in CRCA and much smaller than the cyclobutene $C_4H_4$ unit in CBDC. To summarize, the record-breaking performance of CRCA can be attributed to the ideal arrangement of dense dipoles; that is, the effective addition of ionic and $\pi$-bond polarizations, the highest spatial density of protons, and spatially dense PTM fragments extending across nearly the whole $C_5O_5$ core.

This study has established a number of useful tools for the further development of organic ferroelectric materials: molecular design principles, structural assessment, theoretical simulation, and optimization procedures considering DW dynamics. Our results indicate that the optimization of molecular, crystal, electronic, and/or domain structures may yield further insights toward achieving higher performance, new functionalities, and useful applications of organic systems.

## References

[1] S. Horiuchi et al., Nature Commun., **8**, 14426 (2017).
[2] Y. Noda et al., Adv. Mater. **27**, 6475–6481 (2015).
[3] S. Horiuchi et al. Nature **463**, 789–792 (2010).